Universiteit
Leiden
The Netherlands

Cavity quantum electrodynamics with quantum dots in microcavities

Bakker, M.P.

Citation

Bakker, M. P. (2015, June 17). *Cavity quantum electrodynamics with quantum dots in microcavities*. *Casimir PhD Series*. Retrieved from https://hdl.handle.net/1887/33240

Version:	Not Applicable (or Unknown)
License:	Licence agreement concerning inclusion of doctoral thesis in the Institutional Repository of the University of Leiden
Downloaded from:	https://hdl.handle.net/1887/33240

Note: To cite this publication please use the final published version (if applicable).

Cover Page

Universiteit Leiden

The handle http://hdl.handle.net/1887/33240 holds various files of this Leiden University dissertation

Author: Bakker, Morten
Title: Cavity quantum electrodynamics with quantum dots in microcavities
Issue Date: 2015-06-17

Chapter 2

Experimental setup and sample characterization

In this chapter we will introduce the cryostat and discuss the optical techniques that were used during the low temperature experiments in Chapters 6-8. Next, the sample design and the various design parameters are discussed. Finally, we will discuss the quantum dot growth, energy level schemes and characterization.

2.1 Cryostat

There were 4 key requirements when designing and building-up the cryostat system: (i) have access to both reflection and transmission, as this is required for spatial spin-photon entanglement schemes, (iii) apply an in-plane magnetic field, necessary for spin preparation and manipulation, (iii) have optics outside of the cryostat, as this eases alignment and the micropillars have a small NA < 0.4, (iv) have a closed-cycle system in order to keep the sample cold for longer periods. In the following we will describe the setup that meets all these requirements.

The cryostat that we use is a custom-built *SHI-4XG-S* from Janis Research Co. Drawings of the cryostat and the cryostat mount are displayed in Fig. 2.1. It is a closed cycle exchange-gas vibration isolated cryostat system equiped with a Grifford-McMahon RDK-408D2 Sumitomo cold head, with 1 W cooling power at 4.2 K. It has a cool-down time of about 2 hours to reach the base temperature of 9 K. The 'snout' at the bottom of the cryostat, in which the sample is mounted, is custom-built and has two windows at both sides of the sample with a window–window distance of 19.1 mm and an outer width of 38.1 mm. This window–window distance enables objectives outside of the cryostat to be used at both sides of the sample with working distances of 20 mm, while the outer width of 3 cm makes it possible to place the 'snout' between the poles of an external electromagnet.

The cryostat is mounted on top of an electromagnet (Alpha Magnetics Model 4800 adjustable gap C-frame electromagnet) which, when operated at a maximum current $I_B = 50$ A (Delta Electronics SM45-70D power supply), can produce a maximum in-plane magnetic field of about 1 T at the sample. Vibration isolation is achieved by preventing any rigid mechanical contact

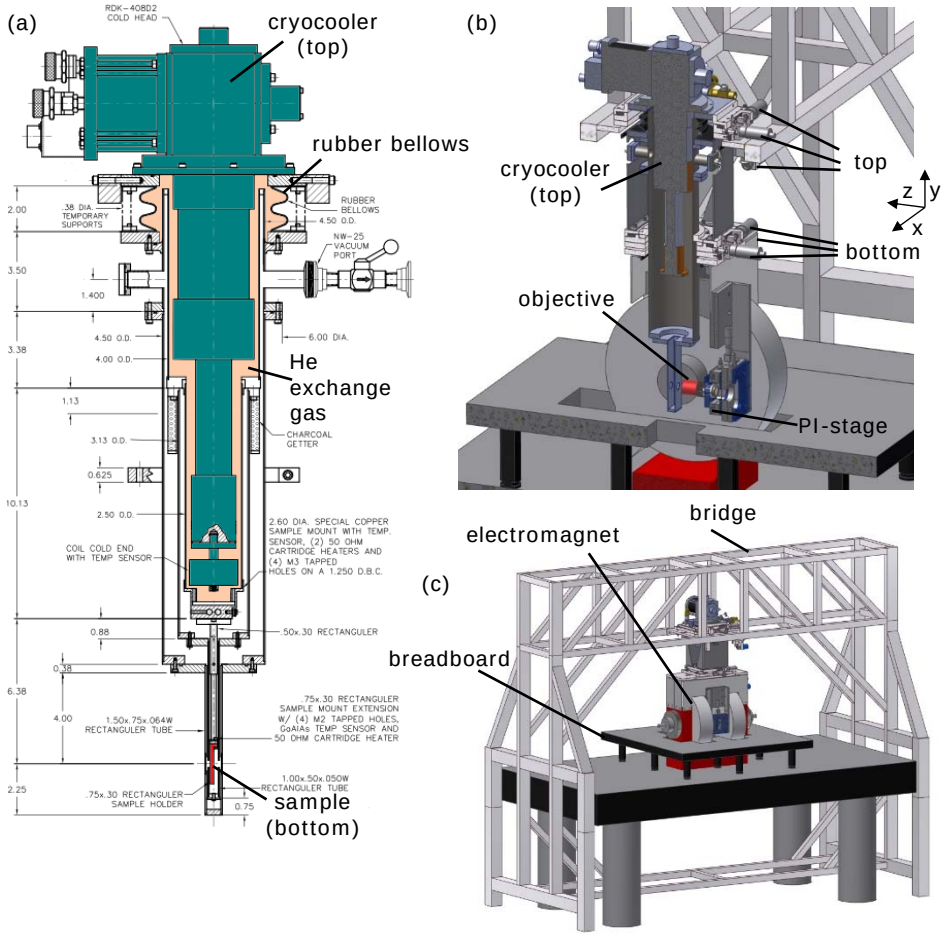

Figure 2.1: Drawings of the cryostat and the cryostat mount. (a) Technical cross-sectional drawing of the cryostat. The cryocooler (top part of the cryostat) and the sample (in the bottom part) are thermally connected with He exchange gas and mechanically only with a rubber bellows. (b) Cross-sectional drawing of a part of the cryostat mount. The cryocooler (top) and the sample (bottom) can be independently displaced in xyz-directions (tuning nobs indicated by lines). Only the front-side objective mounted on a piezo translation (PI) stage is shown. (c) Drawing of the entire cryostat mount, showing the 'bridge' to which the top part of the cryostat is attached, and the electromagnet, breadboard, and optical table on which the bottom part is mounted. [Courtesy of Gijs Verdoes and the Fine Mechanical Department].

between the cryocooler and the sample. Thermal contact is provided by He exchange gas between the cryocooler and the bottom part of the cryostat, which is at atmospheric pressure and enclosed by a flexible rubber bellows that reduces the transfer of vibrations. To reduce pressure changes of the He gas during every ~ 1 Hz cooling cycle, the exchange gas chamber is connected to a He balloon that can easily expand and contract. Furthermore, the bottom part of the cryostat, with the sample, is placed on top of the electromagnet and on the optical table to ensure damping, while the top part of the cryostat, with the cryocooler, is connected via a bridge to the floor of the lab. To study different parts of the sample easily, the bottom and top parts can be independently displaced over several mms in the xyz-directions.

Several low frequency Ph-Br cables are present in order to apply a DC voltage bias (typically 3 wires are used to apply a voltage to two micropillar arrays that share one common ground). A Keithley 2401 sourcemeter is used together with a 7 Hz low-pass filter to prevent high frequency noise to be transferred to the sample. High frequency type-SR coax cables are also present and might be used in future research. As the electromagnet heats up and thermally expands when operated at full power, the cryostat gets vertically displaced. In order to prevent severe misalignment, the frontside objective is mounted directly to the cryostat, such that it gets displaced synchronously. This way, the vertical micrometer-scale displacement takes place in the far field which is less critical than displacements in the near field. The objective is mounted on a PI P–733.3CL stage which enables precise positioning over a xyz $100 \times 100 \times 10$ μm range.

One major disadvantage of the system is that the cryocooler reaches a temperature of 3.5 K and causes He exchange gas to condense. Liquid He then makes a hydraulic contact between the cryocooler and the bottom part, causing vibrations at the sample. Also, He gas then has to be continuously added in order to keep the He exchange gas chamber at atmospheric pressure, otherwise the rubber bellows collapses and causes a rigid mechanical contact. In order to prevent all this the bottom part of the cryostat is kept at a temperature of 9.0 K (Lakeshore 336 temperature controller). In the future we wish to install a heater directly on the cryocooler and keep it at a temperature of 4.5-5 K, hoping that this enables lower sample temperatures. In the original cryostat design, the sample is connected via a relatively long vertical arm to the outside of the cryostat, which is sturdily mounted to the table, and is therefore relatively sensitive to vibrations. We were able to improve this significantly with a thermally isolating, plastic rigid spring between the coldfinger and the inner heatshield. In the future we are considering to

also add a rigid plastic spring between the inner heat shield and the outer heatshield, to further reduce vibrations.

2.2 Optical setup

The sample can be optically studied from two sides (reflection and transmission path) using two objectives (Mutitoyo, 20 mm working distance, 0.40 NA). Several types of experiments were performed throughout this thesis. Photoluminescence measurements and reflectivity measurements, either with a broadband light source or with single-wavelength 1064 nm laser, were performed with a relatively simple confocal setup and, for some experiments, were performed as function of position by spatially scanning the objective. In this section we will discuss four slightly more complicated experiments, namely with one resonant scanning laser, two resonant scanning lasers, one resonant laser and one off-resonant chopped laser, and interference measurements. We will briefly discuss these setups, that are schematically depicted in Fig. 2.2. All experiments are performed with a DAQ card (NI PCI-6259) that controls all the scanning lasers and reads out all the different photodetectors.

2.2.1 One resonant scanning laser

Measuring with one resonant scanning laser is the 'workhorse' technique and results are demonstrated in Chapters 6-8. Also, in order to quickly check whether there are interesting QDs coupled to a specific microcavity, scans with one laser are analyzed on an oscilloscope such that QDs can be viewed as function of bias voltage in 'real-time'.

The setup to perform scans with one resonant laser consists of two modular components, shown in Fig. 2.2 (a,b). The first part, Fig. 2.2 (a), serves to monitor the frequency and intensity of the scanning laser and to set the intensity. A laser (New Focus, Velocity, model 6319, 930-945 nm) is scanned by applying an external voltage. Using beamsplitters part of the laser light is directed to two Fabry-Perot interferometers (FP), with photodetectors (PD) to monitor the transmission, and to a PD to monitor the intensity for normalization purposes. A fine FP (free spectral range 250 MHz , finesse ~ 6) is used to accurately calibrate the frequency scale as function of the external voltage applied to the laser, while the coarse FP (free spectral range 4 GHz, finesse ~ 250) is used to overlay forward and backward frequency scans. A variable attenuation is applied and the light is coupled into a fiber coupler.

The second part of the optical setup, Fig. 2.2 (b), is used to couple the laser into the cavity mode and monitor the reflection and transmission intensities. The light is first coupled out of a fiber coupler, and is coupled in and out of the cavity using free-space optics. The transmitted and reflected light is coupled

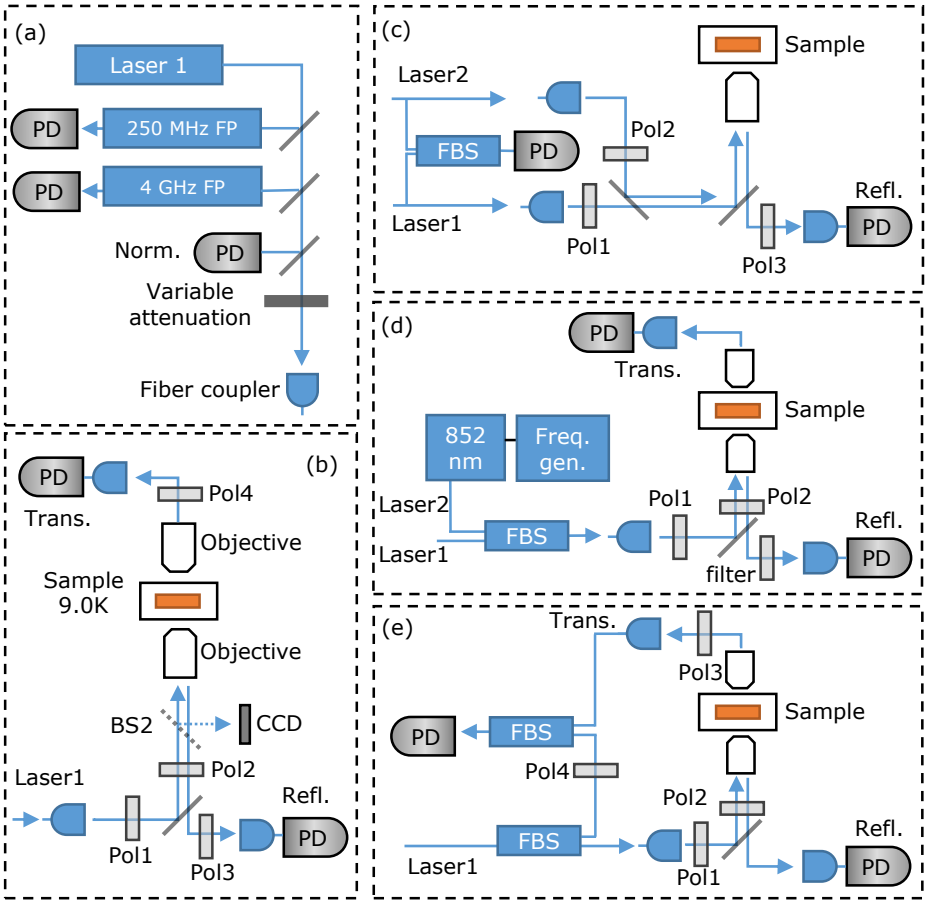

Figure 2.2: Schematic diagrams of the optical setups used throughout this thesis. (a) Setup used when scanning a single laser. PD: photodiode. FP: Fabry-Perot interferometer. Norm: normalization channel. (b) Setup when scanning a single laser and monitoring the reflection and transmission intensities. Pol.: polarizing optics. CCD: CCD-camera. (c) Setup for two lasers experiments. FBS: fiber beamsplitter. (d) Setup used for one resonant laser and one chopped off-resonant (λ =852 nm) laser experiments. Freq. gen.: frequency generator. Filter: 900 nm longpass filter. (e) Setup used for the interference measurements. See main text for more detailed descriptions.

back into a fiber such that it can be easily connected to a high power > 1 μW PD (typically Thorlabs PDA100A Si switchable gain detector), an intermediate power 0.5-8 nW photoreceiver (New Focus 2151 Femtowatt photoreceiver), or a low intensity 1 pW - 100 pW avalanche photodetector (APD). Polarizing optics is used in four places: (i) after the first output fiber coupler (POL1), to control the intensity and match one of the optical axis of the beamsplitter, (ii) in front of the objective (POL2), to set the incoming polarization, and (iii,iv) in the collection paths of the reflected (POL3) and transmitted (POL4) light. In order to image the sample surface we use a CCD camera with in front of it a lens ($f = 100$ mm), together with a beamsplitter (BS2) that can be easily removed.

For alignment purposes it is important to mode match the input and output paths independently, which is not that straight forward as the reflection path forms a confocal setup. Therefore, first the input coupling is optimized by collecting, and maximizing, the transmitted signal with a large area free-space PD. Then, the transmitted light is coupled into a fiber. Finally the reflection channel is mode matched, by exciting the sample with a 852 nm laserdiode (Thorlabs LP852-SF30) and analyzing the photoluminescence (PL) with a fiber coupled spectrometer (resolution 0.019 nm). The PL signal from the fundamental cavity mode is then optimized, and thereby the reflection channel.

For the fibers we typically use APC (angled physical contact) single mode fibers to avoid interference effects due to reflection from the fiber facets, compared to 'flat' PC (physical contact) fibers. Sometimes a multi-mode fiber can also be used in the transmission path, as this fiber is easier to align. For the fiber couplers xyz flexure stages (Elliot Scientific) are used, together with aspheric lenses (typically C240-TME-B, $f = 8.0$ mm).

2.2.2 Two resonant scanning lasers

Scans with two resonant lasers were performed in Chapter 7, where one pump laser was scanned in steps over the cavity resonance and a probe laser was scanned over the whole cavity range during each step. These measurements were crucial in unraveling the dynamical charging effects, but a similar technique could in principle also be used in the future for optical pumping, coherent population trapping, and other experiments.

The setup to perform scans with two resonant lasers is shown in Fig. 2.2 (c). A second laser is added (Toptica, DL Pro, 915-985 nm) that can also be scanned by applying an external voltage. Typically, the Toptica laser is scanned in steps and during each step the Velocity laser is scanned over the full frequency range. In order to have an indication of the relative frequency difference, light from the two lasers is combined using a fiber beamsplitter

(FBS) and the output intensity is monitored with a PD (Thorlabs, PDA-10A, 150 MHz) with a ∼1 kHz high frequency pass filter at the output. Only when the two lasers are detuned less than the PD response frequency a beating signal is produced that is slow enough to be recorded, otherwise there is a 0 V signal due to the high-pass filter. Monitoring the beating signal therefore indicates when the two lasers are resonant.

The two lasers are connected to separate fiber couplers and are superimposed using a beamsplitter, which makes it possible to control the polarization of both lasers independently. When the two lasers are polarized linear and orthogonally, a polarizer in the reflection collection path can be used to monitor only one of them. The intensity of the Toptica laser varies significantly when it is scanned over its full frequency range, and therefore additional polarizing optics is used to keep the intensity constant (not shown in figure).

2.2.3 Resonant and off-resonant chopped laser

Measurements with a resonant and an off-resonant chopped laser are displayed in Chapter 7 and were used to study the build-up and decay time dynamics of charges trapped at the oxide aperture.

In Figure 2.2 (d) we show the setup. Light from the resonant Velocity laser and the 852 nm laserdiode are combined using a FBS. The Velocity laser is first set at the cavity frequency by varying the voltage and then locked to one of the fringes of the 250 MHz FP using a PID control loop. The 852 nm light is continuously modulated by applying a square wave with a frequency generator to the 'MOD IN' input (modulation input/analog control) of the laserdiode controller. In order to record only the resonant laser in the reflection channel, a 900 nm longpass filter is used. In the transmission channel no filter is used and therefore the 852 nm laser is monitored, as typically it is operated at a much larger intensity than the Velocity. The DAQ card unfortunately has a varying time delay between the read-out of the two different APD counter channels, which makes it impossible to directly determine the relative timing of the reflection signal with respect to the 852 nm laser pulses. We solved this problem by applying a couple synchronous gating pulses to both APDs at the start of every measurement, and then determine the time delay from the recorded time traces.

2.2.4 Interference measurements

Interference measurements are the main subject in Chapter 8 and on the one hand demonstrate the coherence of scattered light by a QD as function of intensity and QD detuning, and on the other hand enable the QD induced phase shift to be extracted.

The setup to perform interference measurements is schematically sketched in Fig. 2.2 (e). The setup is identical to the one used for the one laser scans in Fig 2.2 (b), except that additionally the transmitted signal is combined with a reference signal from the scanning laser using a FBS and monitored using an APD. In order to interfere the two signals they must have the same polarization, so an additional 3-paddle polarization controller (Pol4) is used for the reference signal to the polarization to the transmission polarization (Pol3).

2.3 Sample and design

Images of the sample are shown in Fig. 2.3. Fig. 2.3 (a) shows an optical image of the sample holder, on which the sample and pieces of a chip carrier for the wire bonds have been glued. Figure 2.3 (b) displays an optical microscope image of a sample glued on a mount with a slit. The 6×7 micropillar array and voltage contacts to the p- and n-doped layers are visible. In Fig. 2.3 (c) a SEM image of the three etched trenches that define a micropillar are visible.

The oxide apertured micropillar design consists of two distributed Bragg reflectors (DBRs), a λ-thick active region containing QDs, and a $3/4\lambda$-thick aperture region. The sample structure with the refractive indices of the various layers and the simulated field intensities, as a function of the out-of-plane z-direction, are shown in Fig. 2.4 (a,b). The total sample structure with the exact layer thicknesses can be found in the Appendix.

The sample consists of many components and design considerations, of which we will give an overview: (i) First, we will discuss the DBR design considerations, and show how the mirror reflectivities, the cavity length and maximally achievable cavity Q-factor can be calculated. (ii) Next, we will consider the oxide aperture which provides the in-plane transverse mode confinement. (iii) Then, we will discuss the doped layers and show some typical IV-curves. (iv) Finally, we will discuss the QD growth, the energy level schemes, and characterization using macro- and micro-photoluminescence techniques.

2.3.1 DBR design considerations

Each DBR consists of alternating layers of GaAs and $Al_xGa_{1-x}As$ with a thickness of $(0.25 + 0.5m)\lambda$, where m is an integer, and λ is the vacuum wavelength λ_0 divided by the refractive index n. A wave travelling away from the center of the cavity where the QDs are located, will have a positive reflection amplitude $r = (n_{GaAs} - n_{Al_xGa_{1-x}As})/(n_{GaAs} + n_{Al_xGa_{1-x}As}) > 0$ at the GaAs to $Al_xGa_{1-x}As$ interface, as $n_{GaAs} > n_{Al_xGa_{1-x}As}$. This results in a field maximum at this interface and explains the intensity profile shown in Fig. 2.4 (b). The QDs must be located in a field maximum and therefore

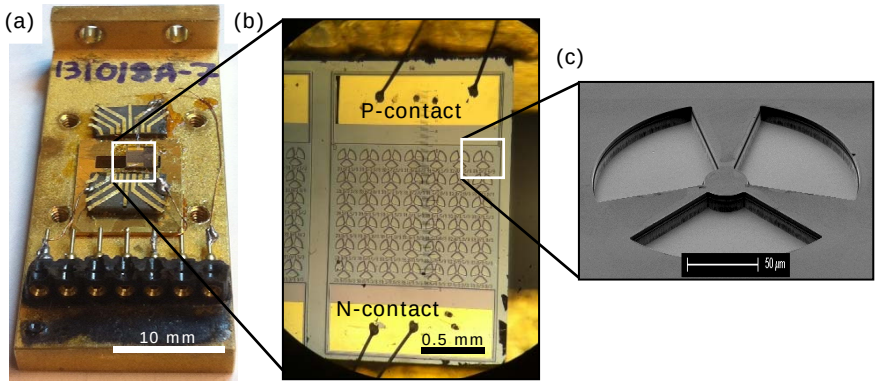

Figure 2.3: Images of a typical sample used for low temperature measurements in this thesis. (a) shows an optical microscope image of the sample on a sample holder, (b) shows the micropillar array and (c) shows a SEM image of a micropillar.

the active region requires a thickness of 1λ. The center of the oxide aperture (consisting of AlAs) is located in a field minimum to minimize light scattering on the oxide, which sets the aperture region thickness to $3/4\lambda$.

The reflectivities of the top R_{top} and bottom R_{bottom} mirrors can be calculated using [101]:

$$R_{top} = \left(\frac{(n_{GaAs})^{2k+1} - n_{vac}(n_{0.9})^{2k}}{(n_{GaAs})^{2k+1} + n_{vac}(n_{0.9})^{2k}} \right)^2$$

$$R_{bottom} = \left(\frac{(n_{GaAs})^{2k+2l+1} - n_{GaAs}(n_{0.9})^{2k}(n_{1.0})^{2l}}{(n_{GaAs})^{2k+2l+1} + n_{GaAs}(n_{0.9})^{2k}(n_{1.0})^{2l}} \right)^2 .$$

The refractive indices at 4 K are given by $n_{GaAs} = 3.478$ for GaAs, $n_{0.9} = 2.979$ for $Al_{0.90}Ga_{0.10}As$, $n_{1.0} = 2.931$ for AlAs, and $n_{vac} = 1$ for vacuum. k, l are the number of $Al_{0.90}Ga_{0.10}As$ and AlAs layers in the top and bottom mirrors. A couple layers of AlAs have been used in the bottom mirror as it gives a larger refractive index contrast and the growth is easier to control than $Al_{0.90}Ga_{0.10}As$ as it is a binary material. It oxidizes much faster than $Al_{0.90}Ga_{0.10}As$, however, and this should be prevented. The sample design that was used in Chapters 5-8 of this thesis consists of $(k = 26, l = 0)$ for the top mirror and $(k = 16, l = 13)$ for the bottom mirror. The number of GaAs layers is equal to $k + l$ for the top mirror and $k + l - 1$ for the bottom mirror, since the top mirror is in contact with vacuum, while the bottom mirror is grown on top of a GaAs substrate. The transmittivity T is simply calculated using $T = 1 - R$, and it follows that $T_{top} = 3.66 \times 10^{-4}$ and $T_{bot} = 3.29 \times 10^{-4}$.

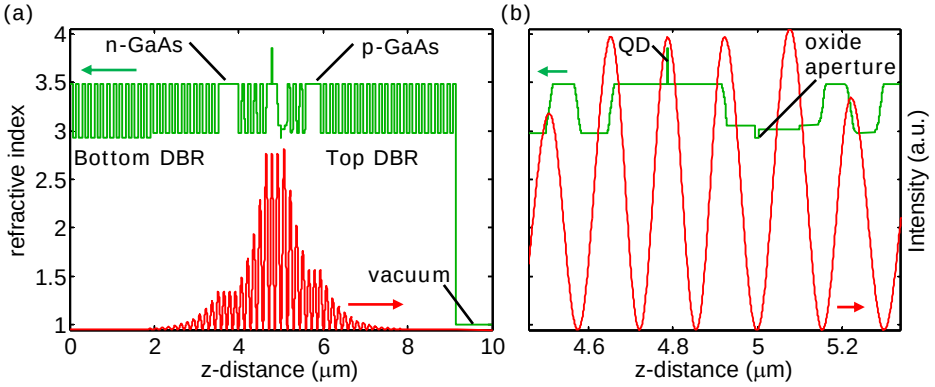

Figure 2.4: Refractive indices and simulated electric field intensities in the sample. (a) shows the total sample structure. The n-GaAs and p-GaAs contact layers are indicated. (b) shows a zoom-in of the central cavity region. Red: electric field intensity. Green: refractive index.

The cavity length is given by: $L = L_{DBR1} + L_{active} + L_{aperture} + L_{DBR2}$, where $L_{DBR1/2}$ is the penetration depth of the top/bottom DBR, L_{active} is the length of the active region and $L_{aperture}$ is the length of the aperture region. The DBR penetration depth is given by [102]: $L_{DBR} = \lambda_0/(4\Delta n)$, where $\Delta n = 0.499$ is the refractive index difference between GaAs and $Al_{0.90}Ga_{0.10}As$. It is more practical to express the cavity length in number of wavelengths $N_\lambda = L\overline{n}/\lambda_0$, where $\overline{n} \approx 3.25$ is the average refractive index. As $L_{active}\overline{n}/\lambda_0 = 1$, $L_{aperture}\overline{n}/\lambda_0 = 0.5$, and $L_{DBR}\overline{n}/\lambda_0 \approx 1.6$, the number of wavelengths is given by $N_\lambda \approx 4.75$.

The mirror loss rate κ_m is calculated using: $\kappa_m = T_{DBR}/t_{round}$, where $t_{round} = 2N_\lambda\lambda_0/c$ is the cavity round trip time. From the above-mentioned values the mirror loss rate is calculated to be $\kappa_{m1} = 12.3$ ns^{-1} for the top mirror and $\kappa_{m2} = 11.1$ ns^{-1} for the bottom mirror. If the cavity Q-factor would only depend on the mirror loss rate, it would be given by $Q = \omega/(\kappa_{m1} + \kappa_{m2}) = 8.6 \times 10^4$.

2.3.2 Oxide aperture

The role of the oxide aperture is schematically depicted in Fig. 2.5 (a). On the one hand it provides in-plane light confinement which, together with the out-of-plane confinement provided by the DBRs (as seen in Fig. 2.4), enables small cavity mode volumes. The confinement potential, which is approximately parabolic, gives rise to Hermite-Gaussian optical modes [103]. These modes can be studied through photoluminescence or reflectivity measurements, both at cryogenic and at room temperatures, as is displayed in

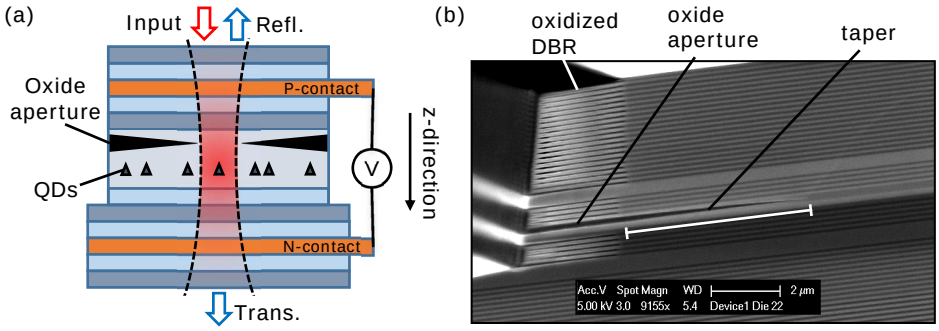

Figure 2.5: Oxide aperture. (a) Schematic drawing of a oxide apertured MP and the Hermite-Gaussian optical mode (number of Bragg pairs and layer thicknesses not to scale). (b) shows a SEM image of the cross-section of an oxidized sample, the tapered oxide aperture and the oxidized $Al_{0.90}Ga_{0.10}As$ in the DBR are indicated.

Chapters 3-5. Additionally, as is displayed in Fig. 2.3 (c), they make it possible to have three 'bridges' that connect the MP to the bulk material in order to enable global voltage contacts.

An oxide aperture is fabricated through the conversion of $Al_xGa_{1-x}As$ to AlO_x during a wet oxidation process. For this, the sample is placed in an oxidation furnace at a temperature of 420 °C and water vapor, carried by N_2 gas, flows around the sample. The wet oxidation is either performed in the home-built oxidation furnace equipped with a viewing port in order to monitor the oxide formation, as is done in Ch. (4,5), or it is performed using the conventional Lindberg furnace in the UCSB cleanroom, as is the case for the samples used in the other chapters. During the conventional UCSB procedure the oxide formation is not monitored, and the exact timing is critical in order to obtain the desired oxide aperture penetration depth. This process is made more accurate by first oxidizing several calibration samples, consisting of etched ridges. The oxidation rate (μm s^{-1}) can then be determined from the SEM image of a cross-section of the sample and is used to determine the oxidation time for the real samples. An example of an image of such a cross-section is presented in Fig. 2.5 (b). As the 10 nm AlAs layer at the center of the aperture region oxidizes faster than the surrounding 66 nm $Al_{0.75}Ga_{0.25}As$ and 95 nm $Al_{0.83}Ga_{0.17}As$ layers, a tapered oxide-aperture is formed, as can be seen in the figure. This taper provides a more gentle confining potential of the transverse optical field compared to a non-tapered aperture, and thereby provides less scattering losses.

2.3.3 Doped layers and voltage contacts

The QDs are embedded inside a PIN diode structure in order to enable deterministic charge control and energy control through the DC Stark shift. The QDs are separated by a 20 nm tunnel barrier from n-doped GaAs and by 110 nm GaAs from p-doped GaAs. For the n-doping Silicon is used and for the p-doping Carbon. Varying doping densities were used as can be seen in the sample structure included in the Appendix.

Countersink etches to the doped GaAs contact layers are made and metal contacts are then applied. The etching occurs through 'Reactive ion etching' during which the reflectivity of a HeNe laser is monitored in order to control the etch depth. To allow some variations in the etch depth, the GaAs contact layers to which the countersink etch is made are thicker, namely $5/4\lambda$ for the p-doped top contact layer and $7/4\lambda$ for the n-doped bottom contact layer. The contact layers are located 3-4 DBR pairs outside of the central cavity region, and therefore both GaAs and $Al_xGa_{1-x}As$ in the DBR are doped. The interface between GaAs and the larger bandgap $Al_{0.90}Ga_{0.10}As$ imposes risk to give rise to a Schottky barrier, which is undesired as it gives an electric field drop that modifies the electric field across the PIN diode as function of the applied bias voltage, and it can act as a charge trap. In order to prevent this the interfaces are graded, meaning that the Al content is linearly or parabolically varied in small steps over ~ 20 nm, and additionally a larger dopant concentration is used at the interfaces.

The metal contact for the p-doped layer consists of Ti-Pt-Au (from bottom to top), and Ni-AuGe-Ni-Au for the n-doped layer. Rapid thermal annealing is used to ensure Ohmic contacts. Figure 2.6 (a,b) shows IV-curves (current measured as function of voltage) of a sample with good contacts made from the 'G130422A' wafer and gives similar results as the 'G131018A' wafer. IV-curves without (blue line) and with (green line) the presence of an additional pump laser are recorded. The pump laser excites charges in the intrinsic region which, in the case of proper Ohmic contacts, are collected and give rise to a more-or-less constant negative current offset. For the blue lines typical diode characteristics are clearly visible. Based on the energy bandgap of GaAs, a turn-on voltage of 1.42 V at room temperature and 1.52 V at 9.0 K is expected. As can be seen in the figure, the obtained values of 0.5 V and 1.0 V are lower, indicating that charges are leaking through the intrinsic region.

The positive voltage bias range, in which QDs are typically optically active, is indicated with the grey shaded area. For smaller voltages, the electric field across the QDs makes optically excited charges tunnel out of the QD before they can optically recombine. For larger voltages, the QD lines appear broader

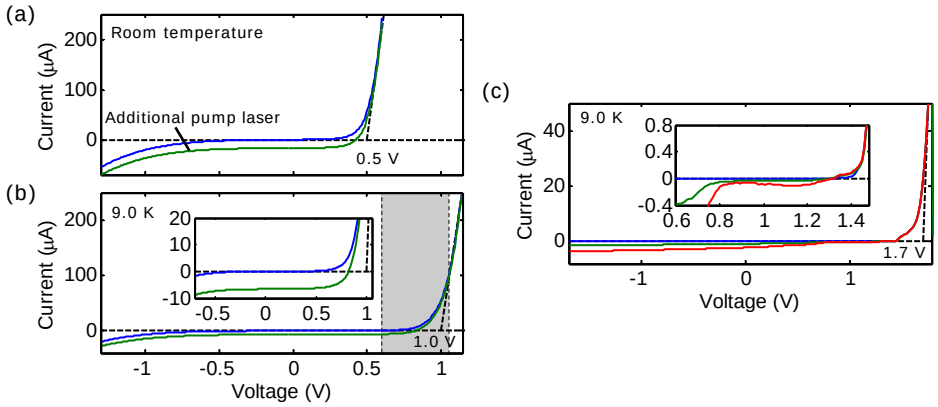

Figure 2.6: IV-characteristics. (a) shows the room temperature IV–curves of a sample from the 'G130422A' wafer without (blue line) and with (green line) the presence of an additional HeNe pump laser. (b) shows the IV–curves of the same sample but cooled down to 9.0 K and using a 780 nm laserdiode pump laser. The grey shaded area indicates the forward bias voltage range where QDs are optically active. (c) demonstrates IV-curves from a sample from the '110207C' wafer without (blue line) and with a 1.2 mW (green line) and 2.3 mW (red line) 852 nm pump laser. The non-uniform current offset that the pump laser induces indicates improper (non-Ohmic) contacts.

and difficult to distinguish from a broadband background photoluminescence, possibly due to the forward bias current.

An example of IV-curves of a sample with improper contacts are shown in Fig. 2.6 (c), which was made from older material ('110207C' wafer). When the sample is not excited (blue line) the IV-curve looks quite typical, albeit with a higher than expected turn-on voltage of 1.7 V. However, the presence of additional pump lasers with increasing intensities (green and red line) give rise to a non-uniform current offset that is strikingly different from what is displayed in Fig. 2.6 (a,b). QDs were still visible in this sample in the voltage range 0.5-1.5 V, but no good charge and energy control was possible. Recording IV-curves without and with the presence of a pump laser therefore serve as a first test on the quality of the contacts, which can be performed before characterizing QD charge and energy tuning.

2.4 Quantum dots

Quantum dots are small semiconductor nanocrystals that confine positive and negative charges in all three dimensions. Charges and excitons therefore exhibit quantum mechanical properties and the allowed energy states are quantized, which leads to discrete optical transitions and QDs are therefore

also called 'artificial atoms'. In the following we will describe their growth, the energy level structure and characterization.

2.4.1 QD growth

Quantum dots are grown by molecular beam epitaxy of In and As on top of a GaAs substrate through a process called Stranski-Krastanov growth, also known as 'layer-plus-island' growth [104]. When less than 1.5 monolayers of InAs are deposited on a GaAs substrate, first a wetting layer is formed. When a thicker layer is deposited, InAs islands are formed to release strain coming from the lattice mismatch between InAs and GaAs. Since we require reasonably high QD densities of $\sim$ 100 μm^{-2}, 1.85 monolayers of InAs are deposited. The growth occurs at a temperature of 500 °C and is accurately monitored using RHEED (Reflection high-energy electron diffraction). Additionally, the partial capping technique is applied, which implies that after the QD growth a $\sim$1 nm GaAs layer is deposited and an annealing step is applied [105]. This ensures a homogeneous $\sim$1 nm QD height and spectral distribution. A STM (scanning tunneling microscopy) image of the cross-section of a QD is shown in Fig. 2.7 (a) and shows how the QD can be seen as a $\sim$ 50 nm diameter lens-shaped InAs droplet inside a GaAs matrix.

In order to determine the QD density and spectral distribution, a calibration sample is grown that contains one layer of encapsulated QDs and on top one layer of uncapped QDs. Figure 2.7 (b) shows an AFM image of the encapsulated QDs on top of a GaAs substrate. From this the QD density is determined to be $\sim$ 110 μm^{-2}. Figure 2.7 (c) shows photoluminescence collected over a large area from the encapsulated QDs. This macro-PL spectrum shows several peaks, of which the largest two are centered at $\lambda = 927$ nm and $\lambda = 950$ nm. These peaks arise most likely from monolayer height fluctuations of the QDs. AFM and macro-PL characterization provides critical information on the spatial and spectral density of the QDs at the cavity mode wavelength, and helps to estimate the chance whether a QD can be found that couples spatially and spectrally with a cavity resonance.

2.4.2 QD level scheme

A QD forms a zero dimensional structure where the energy levels of valence and conduction band electrons are quantized, as InAs has a smaller energy band gap (0.43 eV for bulk InAs at 0 K) compared to the surrounding GaAs matrix (1.52 eV) and because of its small $\sim$nm dimensions. QDs are therefore called 'artificial atoms', as the excitation and recombination of an electron-hole pair, called an exciton, occurs at well-defined energies, while for higher dimensional structures a continuum of energy levels is present. Due to the

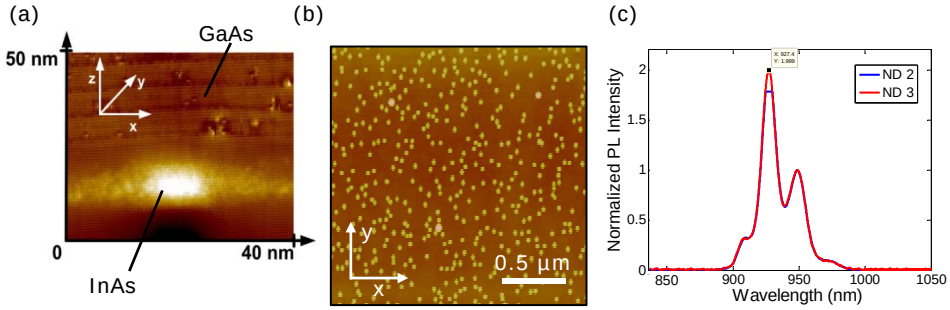

Figure 2.7: Quantum dot characteristics. (a) shows a scanneling tunneling image of the cross-section of a QD [106]. (b) shows an AFM scan of uncapped QDs. (c) shows QD macro-PL. [(b,c) Courtesy of Ajit Barve].

small out-of-plane dimension of the QDs the heavy-hole and light-hole bands are split in energy and the excitation of a heavy-hole spin, which carries spin $S_z = \pm 3/2$, is lowest in energy. By embedding the QDs in a PIN-diode structure, the Fermi energy level E_F, the energy up to which all allowed energy levels are occupied, can be tuned by applying a bias voltage and controls the QD charge occupation.

Figure 2.8 (a) shows the case where the Fermi level is tuned just below the lowest conduction band energy level and the QD is charge neutral. The QD 'empty' ground state $|0\rangle$ can be excited to the $|X^0\rangle$ exciton state. In Fig. 2.8 (b) it is displayed that the exciton has two fine split excited states which can be excited with linearly polarized light (along the xy-direction) of orthogonal polarizations. The fine splitting arises from QD anisotropy in the QD shape, composition, and strain, which leads to electron-hole exchange interaction, and causes the exciton orientation to not be in the out-of-plane direction ($|\uparrow\Downarrow\rangle$ and $|\downarrow\Uparrow\rangle$), but in the in-plane direction.

Figure 2.8 (c) shows the case where the Fermi level is tuned just above the first conduction band level and the QD ground state $|e\rangle$ and excited state $|X^{1-}\rangle$ are singly-charged. Coulomb repulsion energy ensures that the QD is not doubly-charged. In Fig. 2.8 (d) the energy level scheme is displayed in the absence of an external magnetic field. The ground state spin up $|\uparrow\rangle$ and spin down $|\downarrow\rangle$ states, carrying spin $S_z = \pm 1/2$, can be excited with circularly polarized transitions to the corresponding excited states carrying spin $S_z = \pm 3/2$. The relevant energy levels for the case where an in-plane magnetic field B_x is applied is shown in Fig. 2.8 (e), where the spin states are now oriented in the same in-plane x-direction. Even though this configuration was not investigated thoroughly during the time of this thesis, it is important for quantum information applications, as it enables among others high-fidelity

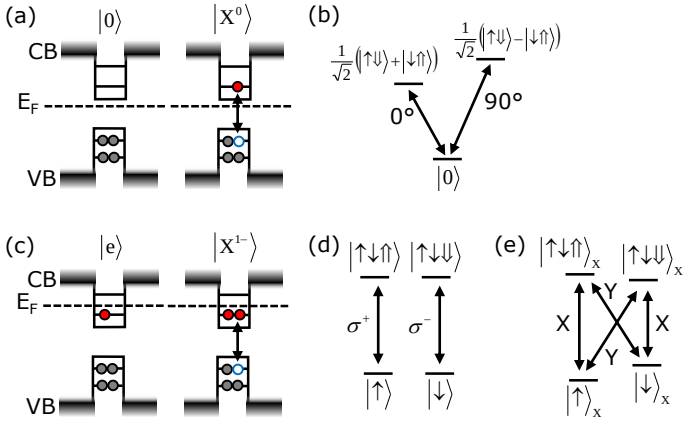

Figure 2.8: Schematics of quantum dot energy levels. (a) shows schematically the ground state $|0\rangle$ and excited state $|X^0\rangle$ of a charge neutral QD. E_F: Fermi level, CB: conduction band, VB: valence band. (b) shows the relevant energy level scheme, where the fine split excited states can be excited with orthogonally linearly polarized transitions. (c) displays schematically the ground state $|e\rangle$ and excited state $|X^{1-}\rangle$ of a singly-charged QD. (d) displays the energy levels without an external magnetic field and (e) shows the case where an in-plane magnetic field B_x along the x-direction is applied. The ground and excited states are coupled by circularly polarized transitions (σ^+, σ^-) or linearly polarized transitions in the x- or y-direction (X,Y).

spin state preparation [107, 108], coherent population trapping [106, 109], and optical manipulation [72–74].

2.4.3 QD characterization

In order to characterize the charge and DC Stark shift tuning of individual QDs, the sample is excited non-resonantly with a $\lambda = 852$ nm laser and photoluminescence is collected as function of wavelength from a small spot size (micro-PL) on a contacted sample. An excellent area to probe micro-PL in a micropillar sample is the region around the top metal contact, as here the top mirror is almost completely etched away and a low Q cavity provides a wide spectral window to view individual QDs. Spatial scans of micro-PL collected at different wavelengths is shown in Fig. 2.9 (a,b), where single QDs are clearly visible as point-like emitters. Figure 2.9 (c) shows micro-PL recorded as function of voltage. Individual QD lines are visible that show a DC Stark shift and charge tuning. In the voltage range 0.65-0.85 V the QDs are neutral, while above 0.85 V the QDs are singly negatively charged. The charged state of the QDs can be determined by analyzing the PL as function of the collected polarization. As is shown in Fig. 2.9 (d) for a charge neutral

QD, two fine-split transitions with linear orthogonal polarizations are visible. PL from a singly charged QD, presented in Fig. 2.9 (e), does not display this fine-splitting.

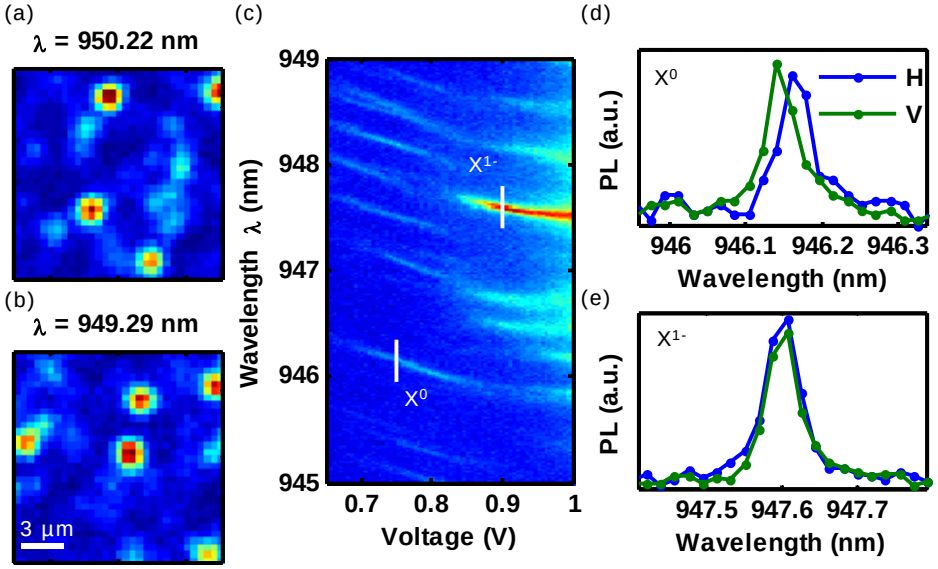

Figure 2.9: Micro-photoluminescence using off-resonant excitation (λ = 852 nm) on individual quantum dots. (a, b) show spatial scans at collection wavelengths labelled in the title. (c) shows the PL intensity as function of the applied bias voltage and the spectrometer wavelength. (d) shows PL at a fixed voltage as function of two linear orthogonal polarizations, showing the fine structure splitting of a neutral QD (X^0). (e) shows the PL for the same two polarizations for a singly-charged QD. White lines in (c) indicate the voltage and wavelength range that (d,e) are recorded.